UC Irvine
UC Irvine Previously Published Works

Title

Optical low-coherence reflectometry to enhance monte Carlo modeling of skin

Permalink

https://escholarship.org/uc/item/1r28v9sm

Journal

Journal of Biomedical Optics, 2(2)

ISSN

1083-3668

Authors

Barton, Jennifer K
Milner, Thomas E
Pfefer, T Joshua
et al.

Publication Date

1997

DOI

10.1117/12.268957

Copyright Information

Peer reviewed

Optical Low-Coherence Reflectometry to Enhance Monte Carlo Modeling of Skin

Jennifer Kehlet Barton,[†] Thomas E. Milner,[‡] T. Joshua Pfefer,[†] J. Stuart Nelson,[‡] and Ashley J. Welch[†]

[†]University of Texas at Austin, Biomedical Engineering Department, Austin, Texas 78712; [‡]University of California Irvine, Beckman Laser Institute and Medical Clinic, Irvine, California 92612

Abstract

Optical low-coherence reflectometry and confocal microscopy images were taken of the rat dorsal skin flap window model. Blood vessel depths and diameters measured with the two techniques, and preparation thickness determined from reflectometry images, are in reasonable agreement with measurements from histologic sections. Blood vessels appear as areas of low signal when constant-depth reflectometry images are taken at a depth near the center of a vessel, whereas they appear bright when taken close to the blood–dermis boundary. Doppler shift plus increased light absorption in blood, and the blood–dermis index of refraction mismatch, are discussed as possible causes of the dark- and bright-appearing vessels, respectively. One reflectometry image was used to generate an input grid for a novel Monte Carlo analysis program that is capable of determining the light distribution and heat generation [J/m^3] within complex blood vessel geometries. The feasibility of imaging skin blood vessel accurately with optical low-coherence tomography, and using the acquired knowledge of blood vessels structure to create more realistic Monte Carlo analyses is demonstrated by the results of the study. © 1997 Society of Photo-Optical Instrumentation Engineers. [S1083-3668(97)00702-8]

Keywords blood vessels; confocal microscopy; laser therapy; port wine stains.

1 Introduction

Optimum laser treatment parameters for vascular disorders such as port wine stains (PWS) are undoubtedly affected by skin blood vessel structure. *In vivo* studies and modeling have suggested that optimum laser treatment parameters of PWS (wavelength, pulse duration, spot size, and pulse energy) depend upon blood vessel depths and diameters, and the number of vessels per unit of dermal volume.[1–6]

Determination of skin blood vessel structure has been hindered by the lack of a suitable measurement technique. Site to site structural variations on the same PWS patient, along with the pain and risk of scarring, make biopsy impractical. The limited optical penetration depth associated with confocal microscopy and transcutaneous microscopy are much less than the required 1 mm, and current ultrasound devices lack the spatial resolution to image the smaller yet clinically significant blood vessels (10 to 70 μm). Optical coherence techniques, including optical low-coherence reflectometry (OLCR), have recently been used to image the structure of both transparent (eye) and turbid (skin) tissues with a resolution of 10 to 20 μm,[7–11] and

with a penetration depth of up to 1.5 mm in skin.[10,11]

Once the blood vessels have been imaged, a method must be employed to translate structural information into optimum laser treatment parameters. Most analyses describing the interaction of laser light with skin have used simplified skin geometries in which the blood vessels are represented by sheets, cylinders, or other regular shapes.[1,3,12,13] In this study, a novel Monte Carlo analysis program has been created that is capable of computing light distribution and heat generation [J/m^3] within the complex blood vessel geometries imaged by OLCR.

A convenient *in vivo* system to study skin microvasculature is provided by the rat dorsal skin flap window model. This system is an outgrowth of various designs for the study of microcirculation, including the rabbit ear[14] and the hamster cheek pouch.[15] The model has been used for microcirculatory studies of cancer growth,[16] and has been adapted to the Syrian golden hamster for studies of laser–tissue interaction.[17] The window model is a chronic (2 to 3-week) preparation that provides a unique opportunity to view a microvasculature field (10 to 300-μm diameter vessels) through a glass window (or directly with the glass removed),

Address all correspondence to Jennifer Barton. E-mail: jbarton@mail.utexas.edu
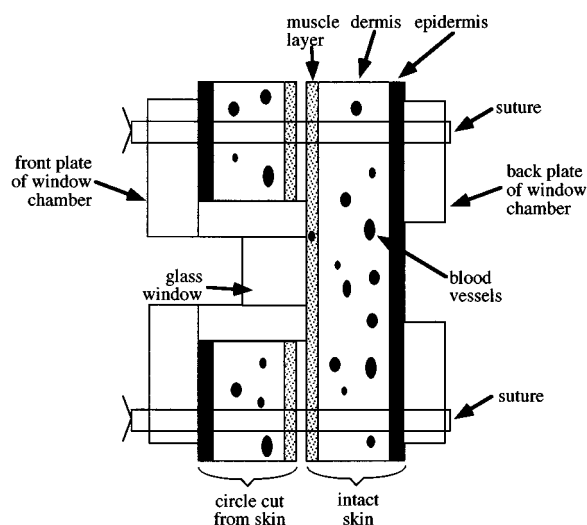
Fig. 1 Cross-section schematic of the rat dorsal skin flap window model preparation. OLCR and confocal microscopy images were obtained from the window side.

while retaining the full thickness of normal skin. The purpose of this study is to test the feasibility of using OLCR and our Monte Carlo analysis program to generate accurate calculations of laser energy deposition in skin.

2 MATERIALS AND METHODS

Sprague-Dawley rats weighing approximately 240 g were implanted with a dorsal skin flap window. A schematic of the preparation is shown in Figure 1. The window is supported by two aluminum plates bolted together and attached surgically to the dorsal skin. The shoulder of each plate is bent to allow the window to rest on the animal's back without tilting. One plate has a housing to accept a 1-cm diameter glass or plastic window, which is affixed in place with an aluminum retaining ring. The implantation procedure is accomplished under anesthesia in sterile conditions. The major steps are:

1. anesthetize the rat with a mixture of xylazine and ketamine (3:4 ratio, 0.1 ml/100 g);

2. shave the hair off the back and remove roots with depilatory;

3. grasp the skin at the dorsal midline, lift, and suture it to a temporary c-clamp;

4. mark the window area and chamber bolt holes on the skin with a template;

5. remove one complete layer of skin and the fascia of the opposing side in the window area (the layer of muscle tissue is left in place), punch holes for chamber bolts;

6. position chamber plates on skin flap, bolt and suture in place; and

7. remove temporary c-clamp, install glass window.

The window model allows imaging of the microvasculature either from the skin (epidermal) or window (dermal) side of the preparation.

The rats were allowed to recover from surgery for 3 days. After recovery, they were anesthetized with xylazine and ketamine (3:4 ratio, 0.1 ml/100 g) and the window covering the dermis was removed. Images were taken of the blood vessels from the dermal side, first with the OLCR system, then with the confocal microscope. The exposed skin was kept moist with phosphate buffered saline solution throughout the experiments.

The OLCR system shown in Figure 2 is similar to one described earlier.[9] Light emitted from a superluminescent diode [$\lambda = 855$ nm, full width half-maximum (FWHM) bandwidth 22 nm] and a He-Ne aiming laser is combined and coupled into one branch of a fiber optic Michelson interferometer. Light is split into two fibers using a 2×2 coupler, one leading to a reference mirror and the second to a probe that focuses light on the tissue. The optical power on the tissue is 300 μW. The optical phase in the reference and sample arms is modulated (180 deg relative phase) at 1000 Hz with piezoelectric cylinders, and stress birefringence is used in the reference arm to match the polarization of the beams and optimize fringe contrast. Light reflected from the reference mirror and backscattered by the sample recombine within the 2×2 coupler. When the optical path length difference between light in the sample and reference arms is within the source coherence length, interference is observed. An AC coupled photovoltaic detector detects interference fringe intensity. The fringe intensity specifies the amplitude of light backscattered from the sample and is measured by a spectrum analyzer with a bandpass of 20 Hz about the 1000 Hz carrier frequency. Measured fringe intensity is digitized and processed via computer to form a two dimensional image of the tissue.

The dynamic range of the OLCR system is 80 dB. Lateral resolution of the system is 5 μm. Axial resolution is determined by the coherence length, which is defined as:[18]

$$L_c = \ln(2)\, \frac{2}{\pi}\, \frac{\lambda^2}{\Delta\lambda}\,, \qquad (1)$$

where λ is the center wavelength and $\Delta\lambda$ the FWHM bandwidth of the superluminescent diode, which for this system gives 14 μm. Images are acquired by performing a series of one-dimensional scans. In this study, scans were taken at 10 μm increments, so the lateral resolution of the images is less than system resolution. Acquisition time varies according to the number and length of the scans; for an image consisting of 100 scans each 1 mm in length, the time is approximately 15 min.

During the OLCR imaging process, the anesthetized rat was placed in a fixture designed to hold the window model rigidly, thus minimizing move-
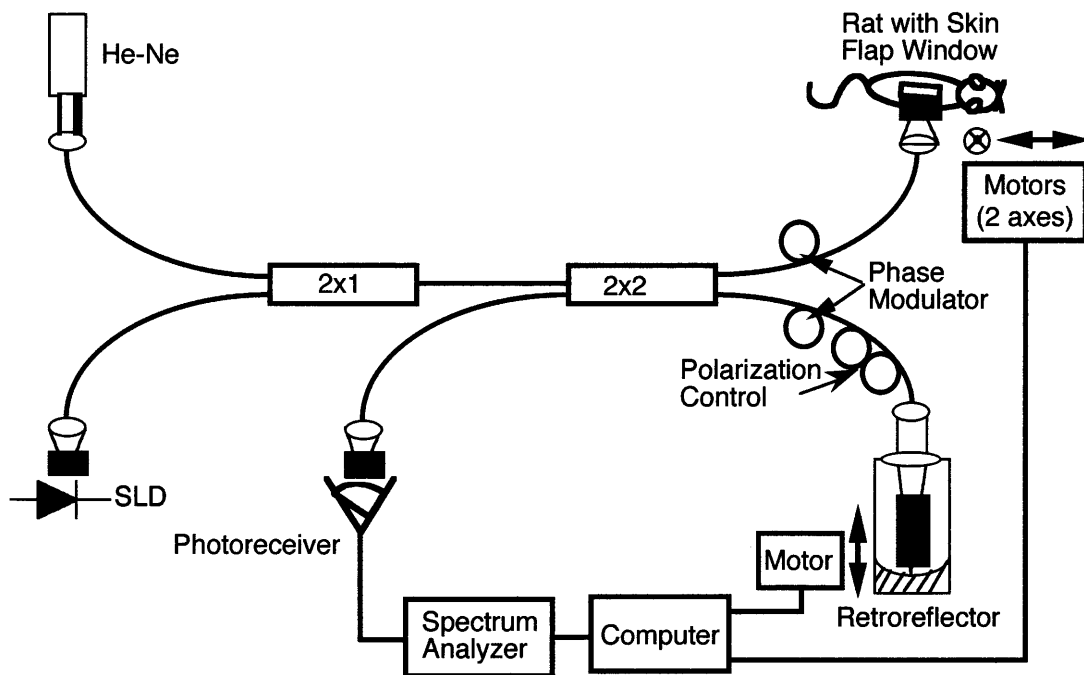
Fig. 2 Optical low-coherence reflectometry system. The SLD has a center wavelength of 855 nm with 300 μW power on tissue.

ment artifacts. Both cross-section (perpendicular to skin surface) and constant-depth (parallel to skin surface) OLCR images were taken. Cross-section images determined the window preparation thickness, and constant-depth images measured the diameter (parallel to the tissue surface) of a prominent blood vessel. For the constant-depth images, the sample probe was tilted 9.8 and 12.4 deg relative to the window in the horizontal and vertical planes, respectively.

The rat was then positioned on the stage of an inverted laser scanning confocal microscope (LSM 410, Zeiss, Oberkocken, Germany). Reflected helium:neon laser light ($\lambda = 543$ nm, maximum output 0.5 mW) images were taken. The reflected light was captured by a photomultiplier tube (R3896, Hamamatsu Corp., Bridgewater, New Jersey) with a sensitivity of approximately 85 mA/W at 543 nm. The objective magnification was $\times 32$. The resolution of the recorded images was 3.2 μm/pixel, which was many times lower than the microscope lateral resolution. The axial resolution of the microscope was approximately 1.6 μm. A series of constant-depth confocal images was taken of the same blood vessel imaged with OLCR, from the surface to the depth at which the signal from blood vessels became indistinguishable from the background noise.

At the end of the experiment, the animal was sacrificed and the window skin removed for histology. The skin was sectioned parallel to the tissue surface for comparison with OLCR and confocal images, and stained with hematoxylin and eosin. The diameter and depth of the blood vessel imaged with

OLCR and confocal microscopy were measured from the histology sections. A photograph of the rat skin flap window is shown in Figure 3. Regions imaged by OLCR and confocal microscopy and pictured in histology are outlined.

The general Monte Carlo procedure for describing laser interaction with layers of homogeneous tissue has been described by Jacques and Wang.[19] Because actual blood vessels are generally too complex to be described by homogeneous layers or simple geometries, the Monte Carlo simulation has been expanded to incorporate a three-dimensional matrix of tissue properties. The matrix spans the extent of the tissue of interest, and every element
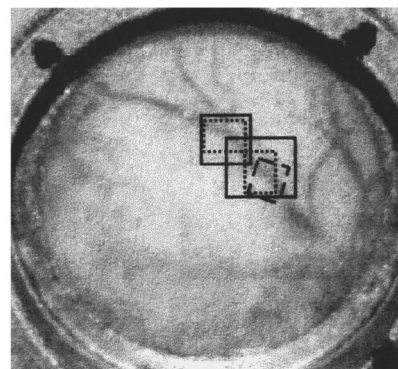

Fig. 3 Photograph of rat skin flap window model. Regions imaged by OLCR (solid lines), confocal microscopy (dashed lines), and shown in histology (dotted lines) are outlined.

(smallest three-dimensional volume defined by the simulation geometry) is assigned a value corresponding to the type of tissue at that location. This allows for arbitrary (within computing capability) complexity in the number of tissue types and the constituent shapes being modeled. The volume element $dx \times dy \times dz$ is adjusted to create a faithful representation of the tissue geometry while minimizing the size of the tissue properties matrix. Another array lists the absorption coefficient, scattering coefficient, anisotropy, and index of refraction for each tissue type.

Photons are propagated through the tissue according to conventional Monte Carlo probabilistic equations. At each step, the position of the photon (x, y, z) is mapped to an element (i, j, k) in the tissue properties matrix. The value of the element is used to determine the type of tissue and the optical properties used in determining photon movement. If the photon has crossed one or more boundaries between tissue types, it is moved back to the first boundary. The photon is then reflected or refracted, and new position, directional cosines, and remaining step size are calculated as appropriate.[20] Following each photon step, the absorption and scattering coefficients of the current tissue type are used to determine the portion of the photon weight absorbed. The photon is then scattered, using the tissue anisotropy to determine the scattering angles (assuming a Heyney–Greenstein scattering function). The photon continues to propagate through the modeled tissue until it is completely absorbed. The absorbed photon weights are accumulated in a photon count matrix, which for simplicity has the same number of elements and element size as the tissue properties matrix. The number of photons absorbed in a tissue volume element is converted to absorbed energy density $[J/cm^3]$. Plots of absorbed energy versus tissue position can be created from specified slices of the three-dimensional photon count matrix.

The tissue properties matrix can be created from a series of histology sections, confocal microscopy images, or OLCR images that sample the entire three-dimensional volume of interest. In this study, the matrix was generated from a single two-dimensional constant depth OLCR image. The image was transferred to the public domain software package NIH Image (National Institutes of Health, Bethesda, Maryland). The imaged blood vessels were identified and manually traced, and their coordinates were used to generate a two-dimensional tissue properties matrix. To expand to a three-dimensional matrix, it was assumed that the blood vessels had circular cross sections and that the OLCR image was taken through the maximum blood vessel diameter.

The optical properties of dermis and blood at 577 nm, as reported in the literature,[12,21] were used in the Monte Carlo analysis program (dermis: μ_a
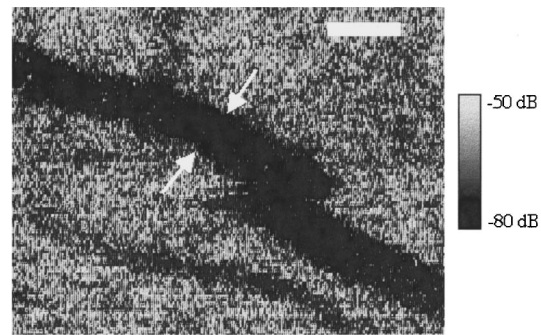

Fig. 4 OLCR image of a straight section of window model blood vessel at a constant depth of 365 μm. Arrows denote position of blood vessel diameter measurement of 196 μm. Bar=250 μm.

$= 2.2$ cm^{-1}, $\mu_s = 131$ cm^{-1}, $g = 0.787$, $n = 1.37$; blood: $\mu_a = 354$ cm^{-1}, $\mu_s = 468$ cm^{-1}, $g = 0.995$, $n = 1.33$).

3 RESULTS

Straight and branching sections of a window model blood vessel were imaged with OLCR. The straight section was also imaged with confocal microscopy. All depths reported are for tissue and are adjusted assuming an average tissue index of refraction of 1.37.

A constant-depth OLCR image of a straight section of blood vessel taken at a depth of 365 μm is shown in Figure 4. A small diameter vessel at the same depth is also observed. In this image, the vessels appear dark, or minimally reflecting compared with the surrounding dermis. The diameter of the large blood vessel was measured from the OLCR image to be 196 μm. A reflected light confocal image of the same straight vessel at a tissue depth of 360 μm is shown in Figure 5. The blood vessel di-
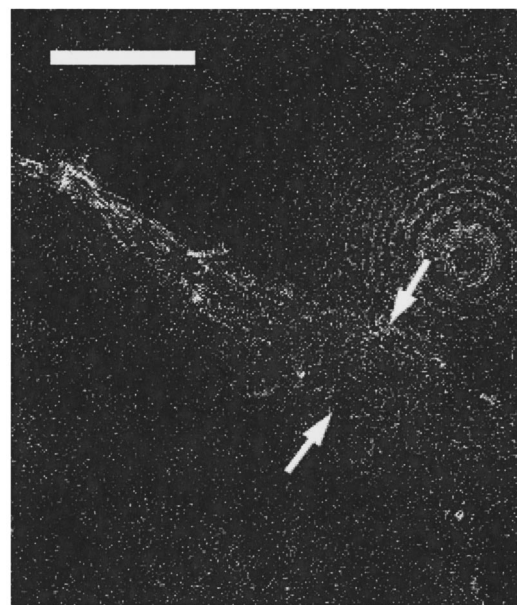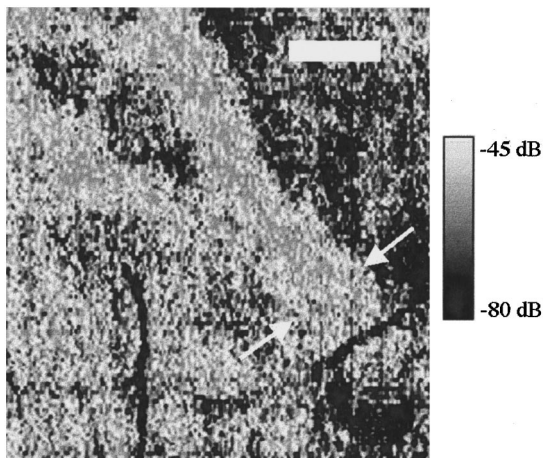

Fig. 5 Reflected light confocal microscopy image at a depth of 360 μm of the same section of blood vessel imaged in Figure 4. Arrows denote position of blood vessel diameter measurement of 176 μm. Bar=250 μm.
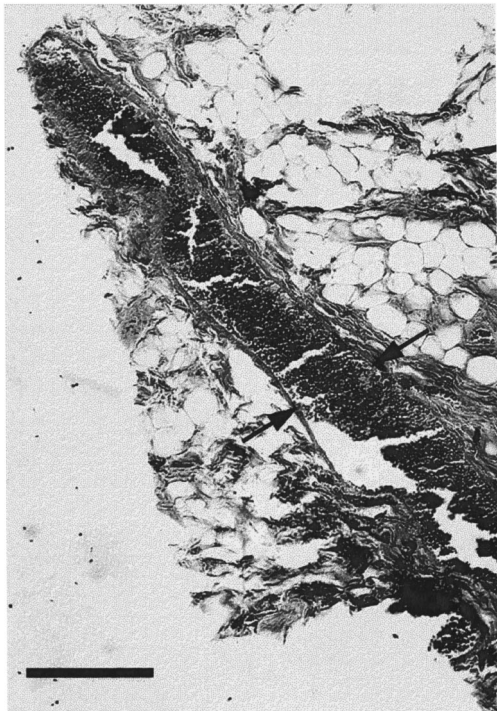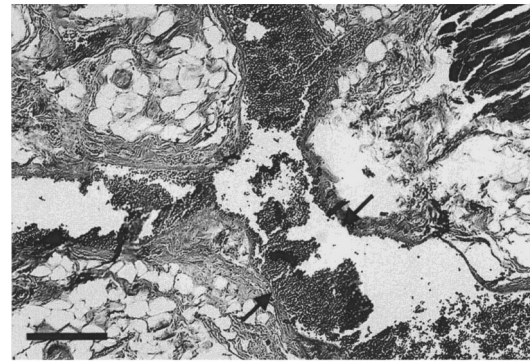
Fig. 6 Histology section at a depth of 390 μm of the blood vessel imaged in Figures 4 and 5. Arrows denote position of blood vessel diameter measurement of 189 μm. Bar=250 μm.
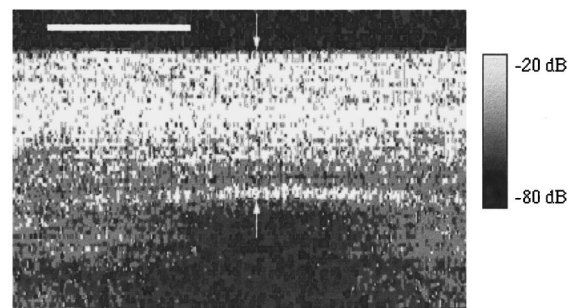

Fig. 8 Histology section at a depth of 362 μm of the same blood vessel imaged in Figure 7. Arrows denote position of blood vessel diameter measurement of 336 μm. Bar=250 μm.

ameter was measured to be 176 μm. A histology section of the same blood vessel is presented in Figure 6. The vessel was visible in histology sections over a depth range of 342 to 438 μm, with the maximum diameter of 189 μm observed at a depth of 390 μm.

An OLCR image of a branching section of the same large vessel at a depth of 328 μm is shown in Figure 7. In this image, the blood vessel appears as a region brighter than the surrounding dermis. The blood vessel diameter before the branch point was

measured to be 290 μm. This image also shows two thin dark curves of approximately 35 μm diameter overlying the large vessel. A histology section of the branching blood vessel is presented in Figure 8. The vessel was visible in sections over a depth range of 316 to 418 μm, with a maximum diameter of 336 μm seen at a depth of 362 μm.

A cross-sectional image of the window model obtained with OLCR is shown in Figure 9. The front and back surfaces of the model are seen as regions of high signal due to changes in the index of refraction between tissue and air. The thickness of the window preparation was measured as 520 μm in this sampled region. The thickness calculated from the number of (constant-depth) histology sections was 522 μm.

The OLCR image in Figure 4 was used to generate the tissue properties matrix of the Monte Carlo program. Deposited energy in the blood vessels and surrounding dermis was calculated using a 1-J/cm^2, 1.0-mm-diameter flat-top laser beam and 10 million photons. Deposited energy is shown in a cross-sectional view at the midpoint of the laser beam (Figure 10) and at a constant depth of 365 μm (Figure 11).

Fig. 7 OLCR image of a branching section of window model blood vessel at a constant depth of 328 μm. Arrows denote position of blood vessel diameter measurement of 290 μm. Bar=250 μm.

Fig. 9 Cross-section OLCR image of the window model. Arrows denote position of thickness measurement of 520 μm. Bar=500 μm.
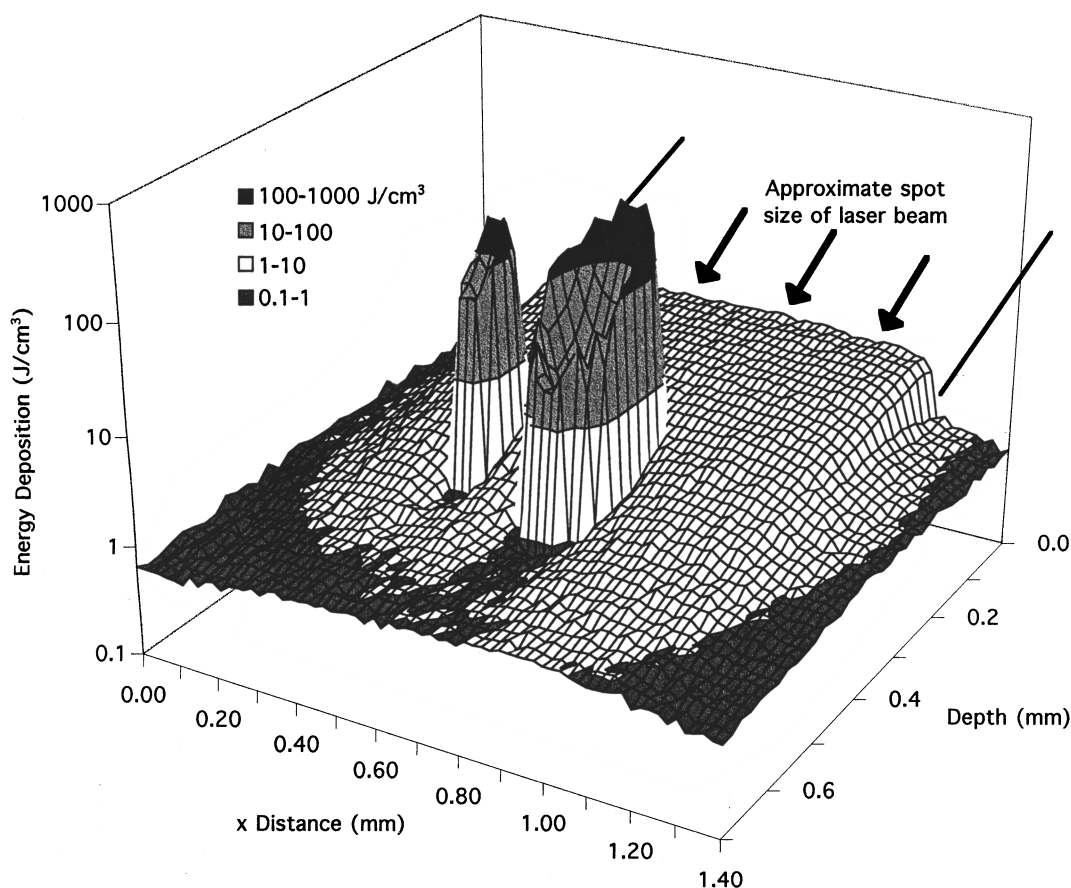
Fig. 10 Cross-section view of deposited energy in blood vessels and dermis generated from Monte Carlo modeling. Laser parameters: wavelength 577 nm, beam diameter 1 mm (beam extent approximated by lines), beam energy 1 J/cm^2.

4 DISCUSSION

Table 1 summarizes the blood vessel depth and diameter, and window preparation thickness measurements made with the three techniques. At the first imaged location (straight blood vessel), blood vessel diameters measured with OLCR, confocal microscopy and histology are in reasonable agreement. The OLCR and confocal images were taken at depths intersecting the blood vessel as determined by histology. At the second imaged location (branching blood vessel), the diameter of the blood vessel measured with OLCR is considerably smaller than the maximum diameter measured in histology. This may be because the OLCR image was taken near the top surface of the blood vessel, above the position of maximum diameter. Diameter measurements from both OLCR images are complicated by the difficulty of precisely defining the edges of the blood vessel. Further error may be introduced from the estimated locations on the histology sections. Determination of window thickness is more straightforward, and the OLCR and histology measurements are in good agreement. At the location of the vessel branching section, histology reveals small (20 to 42-μm-diameter) blood vessels in

sections shallower than the branching blood vessel. These may be the source of the approximately 35 features evident in Figure 7.

Two phenomena, Doppler shift and blood absorption, can explain the reduced signal amplitude of blood vessels in the OLCR image in Figure 4. Previous investigations have shown[22] that when the incident light is Doppler shifted, the detected signal in the frequency band measured by the spectrum analyzer is reduced. The Doppler shift is given by:

$$\Delta f = \frac{2V \cos(\theta)}{\lambda} \qquad (2)$$

where V is the velocity of blood, θ is the angle between the optical axis of the probe and the blood vessel, and λ is the center wavelength of the superluminescent diode. The angle between the optical axis of the probe and the window blood vessels imaged varied between 74 and 80 deg. Flow in venules and arterioles is generally laminar, and the average flow velocity of window model vessels has been measured at 2 to 10 mm/s.[17] Using the largest angle and slowest flow, an average Doppler shift of 817 Hz is calculated, whereas with the smallest
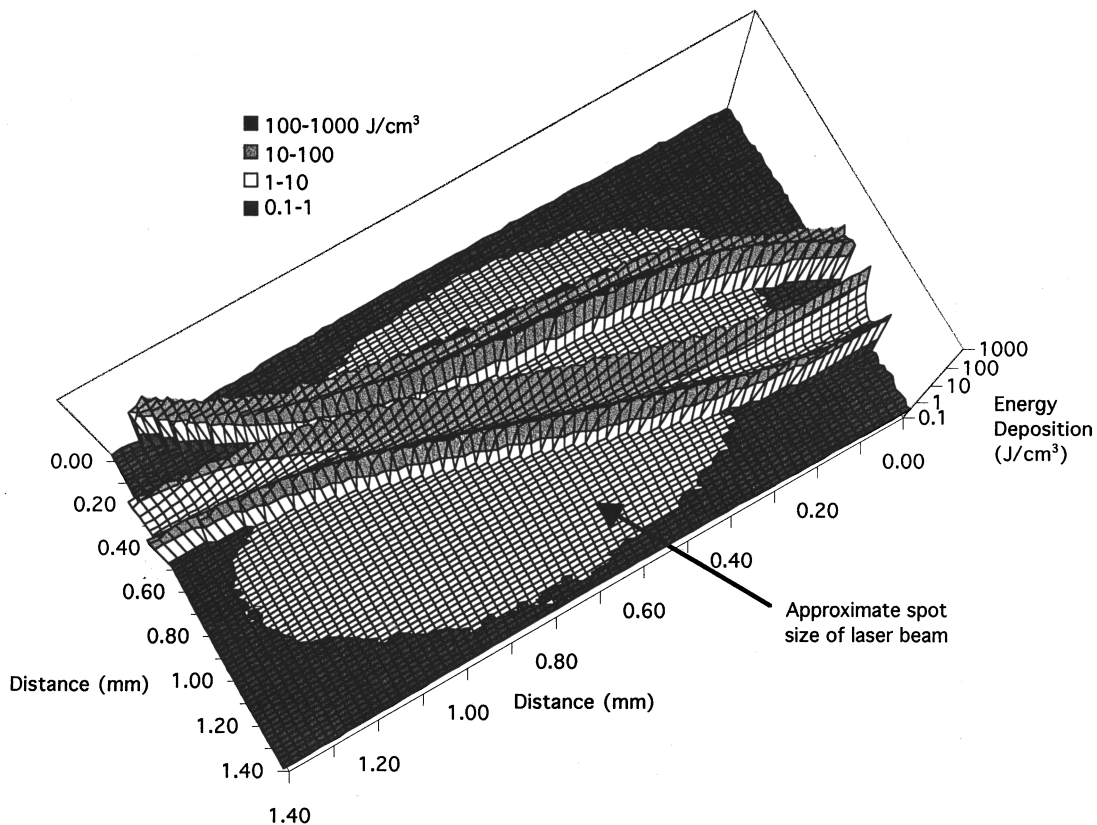
Fig. 11 View of deposited energy in blood vessels and dermis generated from Monte Carlo modeling at a constant depth of 365 μm. Laser parameters: wavelength 577 nm, beam diameter 1 mm, beam energy 1 J/cm². Spot size of laser beam at surface is approximated by the light elliptical area (note differences in scale), which represents energy deposition in the dermis.

angle and fastest flow, an average Doppler shift of 6486 Hz is calculated. The shift at the center of the vessel is expected to be larger and the shift at the periphery of the vessel will approach 0. Since this OLCR image is at a depth well inside the blood vessel, the expected Doppler is many times greater than the bandpass of the spectrum analyzer, which can explain the reduced signal amplitude.

The low signal may also be influenced by the optical properties of blood. At 850 nm, the absorption coefficient of oxyhemoglobin ($\mu_a \sim 7$ cm^{-1} [23]) is greater than that of the surrounding skin ($\mu_a = 0.17$ cm^{-1} [24]). A photon that travels through blood is thus more likely to be extinguished than one that travels an equivalent distance but passes only through the surrounding dermis. Blood vessels are not visible in the OLCR cross-section image of Figure 9, when the probe was normal to the skin surface, indicating that in this study Doppler shift may be more important. The relative contribution of these two phenomena will be quantified in future studies by comparing images of blood vessels taken with tilted and untilted probes, or by stopping the blood flow through the vessels, which would eliminate the Doppler shift.

The OLCR image in Figure 7, however, shows the vessel as an area of high signal. This scan was taken near the shallowest surface of the blood vessel, and thus we believe imaged the boundary between the dermis and blood. Although considerable variation exists in reported values of the index of refraction (n) of blood and dermis, a difference has been re-

Table 1 Measurements of rat dorsal skin flap window model.

Region	OLCR		Confocal microscopy		Histology	
	Depth	Diam.	Depth	Diam.	Depth range	Max diam.
Blood vessel straight	365	196	360	176	342–438	189
Blood vessel, branching	328	290	n/a	n/a	316–418	336
Window thickness	520		n/a		522	

Note: All measurements in micrometers; n/a=not available.

ported at 577 to 590 nm ($n_{blood} = 1.33$, $n_{dermis} = 1.37$).[21] It is expected that this difference would also exist at 850 nm, so that the blood–dermis boundary would be marked by a specular reflection. At the shallowest surface of the vessel, Doppler shift and increased absorption effects are minimized. Histology showed that this vessel is highly elliptical, with a long axis of 335 μm parallel to the tissue surface and a short axis of only 102 μm. These phenomena may explain why the OLCR system imaged this vessel as a bright region 250 μm in diameter.

If the boundary between blood and dermis is marked by a back reflection, a bright curve or ellipse should demarcate the blood vessel in the OLCR cross-sectional image of Figure 9. However, no such feature is apparent. This may be due to the relatively weak signal from the blood–dermis boundary being overwhelmed by the strong air–tissue and random dermal inhomogeneity reflections. Additional studies that include taking a series of cross-section images with a tilted probe will characterize the blood–dermis boundary.

In the confocal microscopy image in Figure 5, only the outline of the large blood vessel is faintly visible, in contrast to the two clearly demarcated blood vessels in the OLCR images. Confocal microscopy has been shown to yield excellent images of papillary dermis capillary loops for depths of up to 150 μm.[25] At a depth of 360 μm, however, the confocal contrast is degraded by light scattering. The quality of the confocal image may be improved somewhat by switching to the same longer, less highly scattered wavelength as the OLCR system. However, coherence techniques have been shown to possess fundamentally superior ability to image absorbing structures in scattering media.[8] The present study supports the idea that with the combination of increased rejection of out-of-focus light and the ability to sense Doppler shift, OLCR is better suited for imaging deep skin blood vessels.

The long acquisition time for each image improved the detected signal strength but necessitated that the animal be under anesthesia to minimize movement. A movement artifact is noticeable in the abrupt horizontal shift of the blood vessel in the middle right section of Figure 4. The OLCR system is being modified to decrease the image acquisition time.

Figures 10 and 11, which show deposited energy calculated with the Monte Carlo model, display several of the characteristics shown in previous conventional programs. At the midpoint of the laser beam, substantially more energy (2 to 3 orders of magnitude) is deposited in the blood than in the surrounding dermis. Light is scattered and attenuated as it travels through the dermis, and is quickly absorbed in the blood. Therefore, more energy is deposited at the periphery of the blood vessels than in the center. The most energy is deposited just be-

low the shallowest surface of the vessel, as seen in Figure 10 for both vessels. In Figure 11, the spot size of the laser beam is approximated by the lighter elliptical area. Note that considerable light is absorbed in portions of the blood vessel outside the laser beam, because of light scattering in the dermis.

Although this example demonstrates the ability of the Monte Carlo model to represent realistic blood vessel geometries, the case given here is obviously fictitious. All blood vessels except those seen in the constant-depth OLCR image of Figure 4 are ignored. Histology shows that the blood vessels are elliptical in cross section, not circular, as is assumed. For realistic modeling, a series of two-dimensional scans must be made. The resulting three-dimensional characterization of blood vessels can be translated into a true, representative matrix of tissue properties for the Monte Carlo model.

5 CONCLUSION

OLCR can be used to image rat window model blood vessels up to a depth of 365 μm with good accuracy. Additional studies are needed to characterize the effects of Doppler shift, blood absorption, and blood–dermis reflections on the images produced. Images through the skin side of the window model will determine the effects of the highly scattering epidermis, and OLCR imaging of blood vessels deeper than about 500 μm will require the use of a different animal model. However, from these experiments, it appears that OLCR is a promising method for accurate measurement of skin blood vessels, and that flexible Monte Carlo modeling can provide estimates of light distribution and absorbed energy for nonuniform representations of blood vessels.

REFERENCES

1. M. J. C. van Gemert, A. J. Welch, J. W. Pickering, O. T. Tan, ''Laser treatment of port wine stains,'' in *Optical-Thermal Response of Laser-Irradiated Tissue*, A. J. Welch and M. J. C. van

Gemert, Eds., Chap. 23, pp. 789–830, Plenum Press, New York (1995).

2. A. J. Welch, J. A. Pearce, K. R. Diller, G. Yoon, and W. F. Cheong, ''Heat generation in laser irradiated tissue,'' *J. Biomech. Eng.* **111**, 62–68 (1989).

3. M. J. C. van Gemert, A. J. Welch, J. W. Pickering, O. T. Tan, and G. H. M. Gijsbers, ''Wavelengths for laser treatment of port wine stains and telangiectasia,'' *Lasers Surg. Med.* **16**, 147–155 (1995).

4. C. C. Dierickx, J. M. Casparian, V. Venugopalan, W. A. Farinelli, and R. R. Anderson, ''Thermal relaxation of port-wine stain vessels probed *in vivo*: the need for 1-10-millisecond laser pulse treatment,'' *J. Invest. Derm.* **105**(5), 709–714 (1995).

5. O. T. Tan, M. Motemedi, A. J. Welch, and A. K. Kurban, ''Spotsize effects on guinea pig skin following pulsed irradiation,'' *J. Invest. Derm.* **90**(6), 877–881 (1988).

6. M. Keijzer, J. W. Pickering, and M. J. C. van Gemert, ''Laser beam diameter for port wine stain treatment,'' *Lasers Surg. Med.* **11**, 601–605 (1991).

7. D. Huang, E. A. Swanson, C. P. Lin, J. S. Schuman, W. G. Stinson, W. Chang, M. R. Hee, T. Flotte, K. Gregory, C. A. Puliafito, and J. G. Fujimoto, ''Optical coherence tomography,'' *Science* **254**, 1178–1181 (1991).

8. J. A. Izatt, M. R. Hee, G. M. Owen, E. A. Swanson, and J. G. Fujimoto, ''Optical coherence microscopy in scattering media,'' *Opt. Lett.* **19**(8), 590–592 (1994).

9. X. J. Wang, T. E. Milner, R. P. Dhond, W. V. Sorin, S. A. Newton, and J. S. Nelson, ''Characterization of human scalp hairs by optical low-coherence reflectometry,'' *Opt. Lett.* **20**(6), 524–526 (1995).

10. J. M. Schmitt, M. J. Yadlowsky, and R. F. Bonner, ''Subsurface imaging of living skin with optical coherence microscopy,'' *Dermatology* **191**, 93–98 (1995).

11. A. Sergeev, V. Gelikonov, G. Gelikonov, F. Feldchtein, K. Pravdenko, D. Shabanov, N. Gladkova, V. Pochinko, V. Zhegalov, G. Dmitriev, I. Vazina, G. Petrova, and N. Nikulin, ''*In vivo* optical coherence tomography of human skin microstructure,'' *Proc. SPIE* **2328**, 144–150 (1994).

12. G. W. Lucassen, W. Verkruysse, M. Keijzer, and M. J. C. van Gemert, ''Light distributions in a port wine stain model containing multiple cylindrical and curved blood vessels,'' *Lasers Surg. Med.* **18**, 345–357 (1996).

13. D. J. Smithies and P. H. Butler, ''Modelling the distribution of laser light in port-wine stains with the Monte Carlo method,'' *Phys. Med. Biol.* **40**, 701–731 (1995).

14. J. C. Sandison, ''The transparent chamber of the rabbit's ear giving a complete description of improved techniques of construction and introduction and general account of growth and behavior of living cells and tissues as seen with the microscope,'' *Am. J. Anat.* **41**, 447–472 (1928).

15. A. G. Sanders and P. Shubik, ''A transparent window for use in the Syrian hamster,'' *Isr. J. Exp. Med.* **11**, 118 (1964).

16. H. D. Papenfuss, J. F. Gross, M. Intaglietta, and F. A. Treese, ''A transparent access chamber for the rat dorsal skin fold,'' *Microvasc. Res.* **18**, 311–318 (1979).

17. Z. F. Gourgouliatos, A. J. Welch, and K. R. Diller, ''Microscopic instrumentation and analysis of laser-tissue interaction in a skin flap model,'' *J. Biomech. Eng.* **113**, 301–307 (1991).

18. E. A. Swanson, D. Huang, M. R. Hee, J. G. Fujimoto, C. P. Lin, and C. A. Puliafito, ''High-speed optical coherence domain reflectometry,'' *Opt. Lett.* **17**(2), 151–153 (1992).

19. S. L. Jacques and L. Wang, ''Monte Carlo modeling of light transport in tissues,'' Chap. 4 in *Optical-Thermal Response of Laser-Irradiated Tissue*, A. J. Welch and M. J. C. van Gemert, Eds., pp. 73–100, Plenum Press, New York (1995).

20. T. J. Pfefer, J. K. Barton, E. K. Chan, M. G. Ducros, B. S. Sorg, and A. J. Welch, ''A three dimensional modular adaptable grid numerical model for light propagation during laser irradiation of skin tissue,'' *J. Select. Top. Quantum Electron.*, in press.

21. W. Verkruysse, J. W. Pickering, J. F. Beek, M. Keijzer, and M. J. C. van Gemert, ''Modelling the effect of wavelength on the pulsed dye laser treatment of port wine stains,'' *Appl. Opt.* **32**, 393–398 (1993).

22. X. J. Wang, T. E. Milner, and J. S. Nelson, ''Fluid flow velocity characterization by optical Doppler tomography,'' *Opt. Lett.* **20**(11), 1337–1339 (1995).

23. A. J. Welch, M. J. C. van Gemert, W. M. Star, and B. C. Wilson, ''Definitions and overview of tissue optics,'' Chap. 2 in *Optical-Thermal Response of Laser-Irradiated Tissue*, A. J. Welch and M. J. C. van Gemert, Eds., p. 34, Plenum Press, New York (1995).

24. W. Cheong, ''Measurement of tissue optical properties: methods and theories,'' ''Appendix to Chap. 8: summary of optical properties,'' Chap. 8A in *Optical-Thermal Response of Laser-Irradiated Tissue*, A. J. Welch and M. J. C. van Gemert, Eds., p. 293, Plenum Press, New York (1995).

25. M. Radjadhyaksha, M. Grossman, D. Esterowitz, R. H. Webb, and R. R. Anderson, ''*In vivo* confocal scanning laser microscopy of human skin: melanin provides strong contrast,'' *J. Invest. Derm.* **104**(6), 946–952 (1995).